# A combined experimental and theoretical study of the supramolecular self-assembly of the natural benzopyran 2,2-dimethyl-3-hydroxy-6-acetyl-chromane and its isomeric benzofuran 10,11-dihydro-10-hydroxytremetone

Diego M. Gil [a, **, 1], E. Lizarraga [b, c], G.A. Echeverría [d, 1], O.E. Piro [d, 1], C.A.N. Catalán [a, 1], A. Ben Altabef [a, *, 1]

[a] INQUINOA (CONICET-UNT), Facultad de Bioquímica, Química y Farmacia, Universidad Nacional de Tucumán, San Lorenzo 456, T4000CAN, San Miguel de Tucumán, Argentina
[b] Fundación Miguel Lillo, Instituto de Fisiología Animal, Miguel Lillo 251, T4000JFE, San Miguel de Tucumán, Argentina
[c] Facultad de Ciencias Naturales e Instituto Miguel Lillo, Universidad Nacional de Tucumán, Miguel Lillo 205, T4000JFE, San Miguel de Tucumán, Argentina
[d] Departamento de Física, Facultad de Ciencias Exactas, Universidad Nacional de La Plata y IFLP (CONICET, CCT-La Plata), C. C. 67, 1900, La Plata, Argentina

## ARTICLE INFO

## ABSTRACT

Epoxidation of 4HMBA, the main metabolite of the medicinal plant Senecionutans, produces an unstable epoxide eventually giving rise to a mixture of four derivatives, three of them previously reported as natural products. The epoxide product easily undergoes an intra-molecular attack of the phenolic hydroxyl against the epoxide group carbons to produce either a benzofuran or a chromane derivative. When dissolved in methanol-water mixture at room temperature the epoxide is completely solvolyzed to give the corresponding diol (hydrolysis) or vicinal hydroxyl-methoxy (methanolysis) derivative. All the compounds involved in the above reactions were characterized by IR, Raman, H NMR and UV–vis spectroscopies, and by mass spectrometry. Density functional theory (DFT) computations were used to optimize the structure conformations. The optimized structures were further subjected to a Natural Bond Orbital (NBO) and electrostatic potentials analysis. The crystal structures of the title compounds (for short, 3 and 4 respectively) were determined by X-ray diffraction methods. Compound 3 crystallizes in the triclinic P-1 space group with a = 6.4289 (6) Å, b = 8.7120 (6) Å, c = 10.952 (1) Å, $\alpha$ = 92.280 (7)°, $\beta$ = 95.738 (7)°, $\gamma$ = 103.973 (7)°, and Z = 2 molecules per unit cell and 4 in the monoclinic P2$_1$/c space group with a = 11.2891 (6) Å, b = 9.1902 (4) Å, c = 12.4272 (7) Å. B = 113.689 (7)°, and Z = 4. In 3 neighboring molecules are linked to each other by OH···O (keto) bonds giving rise to a polymeric structure. In 4 the OH group is a bifurcate H-bond donor. It forms a weak intra-molecular OH···O (furan) bond and also a much stronger inter-molecular O–H···O (keto) bond giving rise to a zig-zag polymeric structure. A detailed analysis of the solid state molecular interactions of compounds 3 and 4 has been performed using Hirshfeld surface analysis and their associated 2D fingerprint plots.

© 2017 Published by Elsevier B.V.

## 1. Introduction

Chromanes and benzofurans are characteristic metabolites of certain tribes of the Asteraceae family [1]. They are frequently found in several widely distributed American genera such as Senecio, Ageratina, Liatris, Encelia, Eupatorium, Baccharis, Verbesina and Flourensia, and have aroused great interest because of their numerous biological activities such as antimicrobial, allergenic, plant growth inhibitory, pro-apoptotic, and anti-proliferative against cancer cell lines [2].

Benzopyrans (chromanes) derivatives and, particularly, those with a 2,2-dimethyl-2H-benzopyran moiety are present in thousands of natural products with a wide range of biological activities [3]. These plant metabolites generally exhibit low cellular toxicity and good membrane permeability which makes them ideal as drug template. Thus, several 2,2-dimethyl-2H-benzopyrans exhibit

powerful antitumor activity [4—6] and HIV-1 reverse transcriptase inhibition [7,8]. Consequently, structural analysis at molecular and supra-molecular levels of natural chromanes is of great interest because they can be used as starting compounds to prepare novel drugs with improved pharmaceutical profile. Recently, we have reported the synthesis and spectroscopic characterization of 6-acetyl-2,2-dimethyl-chromane; this compound was obtained from 4-hydroxy-3-(3-methyl-2-butenyl)-acetophenone (4-HMBA) (1), the main secondary metabolite of *Senecio nutans* (Asteraceae), a medicinal plant of northwestern Argentina [9].

The molecular design intended to mimic the complex structures and processes found in nature is known as "bio-inspired chemistry" or "bio-mimetic chemistry". Several reports have been published on the biosynthetic origin of benzofurans and chromanes in plants where *p*-hydroxyacetophenone derivatives have been proposed as precursors of benzofurans and chromanes [1,10—13]. In this sense we have speculated that 4-HMBA epoxide (2) would be a useful intermediate for synthesizing benzofurans and chromans. In fact, reaction of 4-HMBA (1) with m-CPBA gave a mixture of epoxide 2 (32.6%) together with chromane 3 (20.9%) and benzofuran 4 (40.5%). The latter two compounds derive from an intra-molecular nucleophilic attack of the phenolic hydroxyl at the epoxide carbons. When this mixture was dissolved in methanol-water solution to be analyzed by preparative HPLC, a progressive decrease in the peak corresponding to the epoxide 2 until its complete disappearance and the appearance of two new compounds, later identified as the phenol-diol 5 and the methoxy-derivative 6, was evident after a few days. Clearly phenol-diol 5 and methoxyderivative 6 were formed by solvolysis (hydrolysis and methanolysis, respectively) of epoxide 2. Three of the four compounds obtained in this work were previously reported as natural products, namely 2,2-dimethyl-3-hydroxy-6-acetylchromane (3) in the aerial parts of *Helicrysumstoechas* [14], 10,11-dihydro-10-hydroxytremetone (4) in the leaves of *Fitchiaspeciosa* [15], and 3-(2,3-dihydroxysopentyl) 4-hydroxy-acetophenone (5) in the aerial parts of *Werneriaciliolata* [16]. It should be noted here that all the compounds obtained in this work are racemates whereas both the natural benzofuran 4 and the diol 5 are the left-handed enantiomers [15,16] hence indicating that the reaction is enzymatically controlled in the plant. The optical rotation of natural chromanol 3 was not reported [14].

The present work reports a bio-mimetic synthesis of natural chromanes and benzofurans by epoxidation of the antifungal metabolite 4HMBA (1) [17,18]. The products obtained were characterized using different spectroscopic techniques such as infrared absorption, Raman dispersion, UV—visible, ^{1}H nuclear magnetic resonance (NMR), and mass spectrometry (MS). In addition, for the structural isomers (RS)-2,2-dimethyl-3-hydroxy-6-acetylchroman (3), (RS)-10,11-dihydro-10-hydroxytremetone (4) and (RS)-3-(2,3-dihydroxy-isopentyl)-4-hydroxy-acetophenone (5), the crystal structures have been determined by single crystal X-ray diffraction methods. The experimental data was correlated with theoretical calculations using DFT methods and different basis sets. The intermolecular interactions in the crystal lattice were evaluated through Hirshfeld surface analysis. The geometry of a Hirshfeld surface reflects the relationship between different atoms and intermolecular contacts present in the crystal. These surfaces are supported by 2D fingerprint plots which quantify the nature and type of intermolecular interactions in the solid.

## 2. Experimental

### 2.1. Synthesis

To 4-HMBA (1) (1.224 g) in 30 mL of CHCl3 cooled in ice was added in small portions *m*-chloroperbenzoic acid (MCPBA) (1.184 g,

77%) with magnetic stirring. The progress of the reaction was monitored by TLC. When the reaction was complete (disappearance of the spot corresponding to 4HMBA) the mixture was filtered out and then diluted with 50 mL of CHCl3. The organic layer was washed with 10% Na2SO3 (2 × 10 mL), 5% NaHCO3 (2 × 10 mL) and water (1 × 10 mL). After drying with anhydrous Na2SO4 and solvent evaporation, 768.7 mg of crude residue was obtained. CG-MS analysis showed a mixture constituted (listed by elution order) by 4 (40.5%), unidentified A (3.6%), 3 (20.9%), 2 (32.6%) and unidentified B (2.5%). The residue was dissolved in a mixture of methanol-water (55:45) to be processed by semi-preparative HPLC using a C18 column (5 μ; 10 mm × 250 mm) with methanol-water 55:45 as elution solvent (isocratic), flow at 2.0 mL min$^{-1}$. After a few injections, a progressive decrease in the peak corresponding to the epoxide 2 and the simultaneous appearance of two new compounds later identified as the phenol-diol 5 and the methoxy-derivative 6 was evident. The hydro-methanolic solution was then set aside at room temperature and monitored by HPLC every week. The peak corresponding to epoxide 2 disappeared completely after four weeks and the chromatogram showed four major components which were collected separately to yield (by elution order): 5 (73.5 mg), 6 (34 mg), 4 (173 mg) and 3 (122 mg) (Scheme 1). Chromane 3, benzofuran 4 and phenol-diol 5 were recrystallized from ethanol.

### 2.1.1. Compound 3: 2,2-dimethyl-3-hydroxy-6-acetyl-chromane (racemic)

Needles (122 mg), mp: 102.4 °C (from ethanol).^{1}H NMR (200 MHz, CDCl3) δ 7.75 dd (1H, 9.3 and 2.2 Hz, H-7), 7.73 d (1H, 2.2 Hz, H-5), 6.85 d (9.2 Hz, H-8), 3.86 dd (5.8 and 4.9 Hz, H-3), 3.10dd (1H, 16.8 and 4.9 Hz, H-4a), δ 2.83 dd (1H, 16.8 and 5.8 Hz, H-4b), δ 2.54 s (3H, CH3—CO), δ 2.18 s (br) (1H, OH), δ 1.38 s and 1.35 s (3H each, gem-dimethyl group), in agreement with published data [14]. EIMS: *m/z* (rel. int.%) [M]$^+$ 220 (40), 205 (7), 187 (10), 163 (9), 162 (9), 149 (52), 119 (11), 107 (29), 91 (12), 77 (21), 71 (32), 57 (10), 51 (9), 43 (100).

### 2.1.2. Compound 4: 10,11-dihydro-10-hydroxytremetone (racemic)

Needles (173 mg), mp: 87.1 °C (from ethanol). EIMS: *m/z* (rel. int.%) [M]$^+$ 220 (17), 205 (2), 202 (4), 187 (13), 162 (63), 147 (71), 133 (6), 119 (85), 91 (23), 77 (9), 65 (6), 59 (74), 51 (7), 43 (100). ^{1}H NMR (200 MHz, CDCl3): δ 7.83 s (br) (1H, H-4), 7.81 dd (1H, 8 and 1.5 Hz, H-6), 6.82 d (1H, 8 Hz, H-7), 4.72 t (1H, 9 Hz, H-2), 3.22 d (2H, 9 Hz, H-3a,b), 2.54 s (3H, H-9), 1.25 s and 1.23 s (3H each, H-4′ and H-5) in agreement with published data [15].

### 2.1.3. Compound 5: 3-(2,3-dihydroxy-isopentyl)-4-hydroxy-acetophenone (racemic)

Crystals (73 mg), mp: 135 °C (from ethanol). EIMS: *m/z* (rel. int.%) [M]$^+$ 238 (4), 220 (5), 205 (2), 187 (2), 180 (18), 165 (6), 163 (7), 150 (25), 149 (29), 137 (52), 119 (12), 107 (21), 91 (11), 77 (16), 71 (17), 59 (39), 43 (100). ^{1}H NMR (200 MHz, CDCl3):δ 7.79 d (1H, H-2), 7.70dd (1H, 8.3 and 2.1 Hz, H-6), 6.88 d (1H, 8.3 Hz, H-5), 3.60 dd (1H, 10.3 and 1.4 Hz, H-2′), 2.91 dd (1H, 14 and 1.4 Hz, H-1'a), 2.66 dd (1H, 14 and 10.3 Hz, H-1'b), 2.52 s (3H, H-8), 2.06 br s (1H, OH), 1.37 s and 1.24 s (3H each, H-11 and H-12) (for ^{1}H NMR in CD3OD see Ref. [16]).

### 2.1.4. Compound 6: 3-(2-hydroxy-3-methoxy-isopentyl)-4-hydroxy-acetophenone (racemic)

White solid (34 mg). EIMS: *m/z* (rel. int.%) [M]$^+$ 252 (2), 220 (2), 205 (1), 187 (1.5), 180 (8), 150 (14), 149 (21), 107 (7), 73 (100), 43 (42).^{1}H NMR (200 MHz, CDCl3):δ 7.76dd (1H, 8.2 and 2.1 Hz, H-6), 7.73 d (1H, 2.1 Hz, H-2), 6.94 d (1H, 8.2 Hz, H-5), 3.74 dd (1H, 9.6 and 1.5 Hz, H-2′), 3.24 s (3H, OCH3),2.83dd (1H, 14.5 and 9.6 Hz, H-1'a),
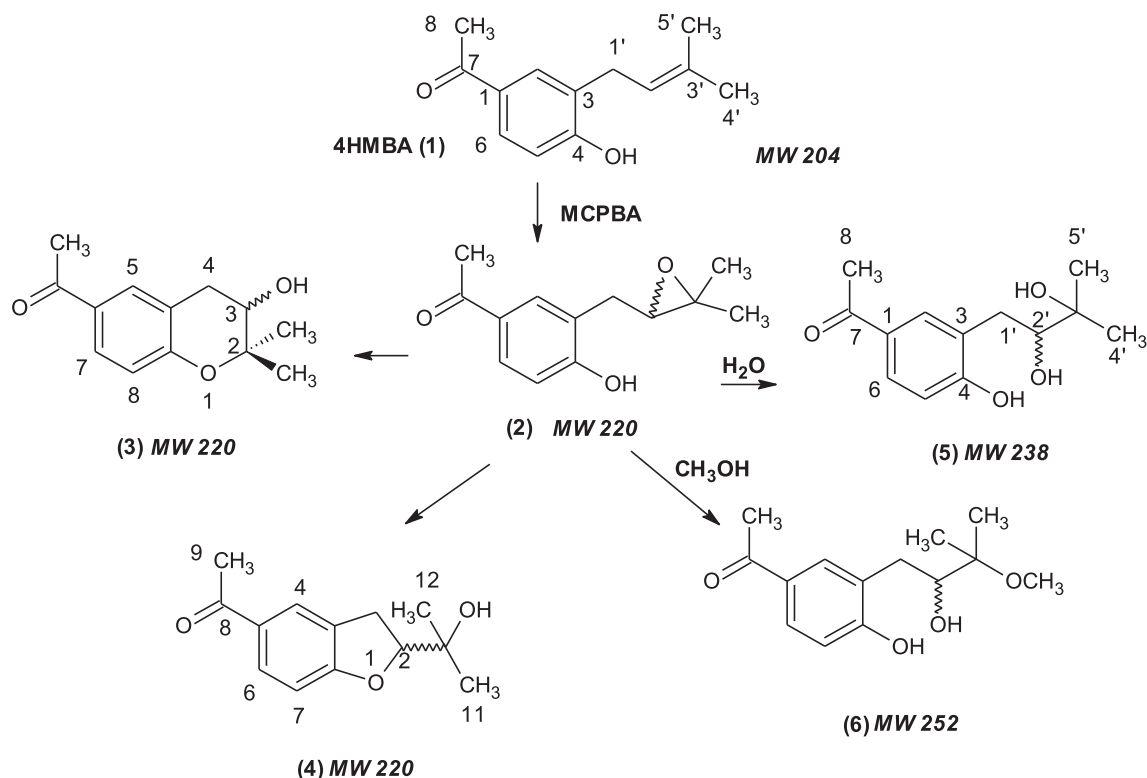
**Scheme 1.** Synthesis of 4HMBA (**1**) derivatives. *Epoxide **2** is unstable at room temperature: a nucleophilic attack of the phenolic hydroxyl at the epoxide carbons yields chromane **3** and benzofuran**4** while dissolution in methanol/water 45:55 gives the solvolysis products **5** and **6**.

2.68dd (1H, 14.5 and 1.5 Hz, H-1'b), 2.54 s (3H, H-8), 1.25 s and 1.20 s (3H each, H-4′ and H-5′); 13C NMR (CDCl3):$\delta$ 197.2 s (C-7), 160.9 s (C-4), 131.7 d (C-2), 129.9 d (C-6), 129.7 s (C-1), 126.2 s (C-3), 117.2 d (C-5), 79.2 d (C-2′), 77.1 s (C-3′), 49.1 q (OCH₃), 34.6 t (C-1′), 26.2 q (C-8), 20.4 q and 18.2 q (C-4′ and C-5′).

## 2.2. Characterization techniques

The crystal melting points were determined using Differential Scanning Calorimetry (DSC) technique. The measurement was performed with a differential scanning calorimeter Perkin Elmer Pyris DSC 6 using 1.150 mg of powdered sample sealed in aluminum pans with a mechanical crimp. Temperature and heat flow calibrations were made with standard samples of indium at its melting transition. Enthalpy changes associated with the melting point of the sample in study ($\Delta$H) were directly obtained from the DSC data by integrating the anomalous peak in the baseline subtracted curve. The entropy change relative to the phase transition was finally determined using the relationship $\Delta S = \Delta H/T$.

^{1}H NMR spectra were recorded on a Bruker AC (200 MHz) spectrometer. Sample was dissolved in CDCl₃ and tetramethylsilane (TMS) was used as internal standard. Chemical shifts were recorded in $\delta$ (ppm) values relative to TMS and $J$ values are expressed in Hertz.

The GC-MS analysis was carried out with a 5973 Hewlett Packard selective mass detector (quadrupole), source 70 eV, coupled to a HP 6890 GC fitted with a HP-5MS column (5% phenylmethylsiloxane, 30 m × 0.25 mm; film thickness 0.25 μm) with helium as carrier gas (1.0 mL/min; constant flow). The oven was programmed for 150 °C (0 min), 150°-180° (3 °C/min) and 234° (3 min). The sample was dissolved in CHCl₂ and the injection volume was 0.1 μL. Injector and detector temperatures were kept at 250 °C and 270 °C, respectively. Injection port was kept at 250 °C,

GC-MS interphase at 275 °C, ion source 230 °C, and MS Quad at 150 °C.

The FTIR absorption spectra of the solid state compounds (in KBr pellets) were recorded in the 4000—400 cm$^{-1}$ region at room temperature on a Perkin-Elmer GX1 Fourier Transform infrared spectrometer with 2 cm$^{-1}$ of spectral resolution. The Raman dispersion spectra of the solids were recorded at room temperature in the 3500—50 cm$^{-1}$ range with a Thermoscientific DXR Raman microscope.

UV—visible spectra were obtained on a Shimadzu 160A spectrophotometer. For this purpose, 6.1 mg of compound **3** and 6.5 mg of compound **4** were dissolved in 10 mL ethanol 96° and from this mother solution appropriate dilutions were obtained with the same solvent. The spectra were recorded between 800 and 200 nm.

## 2.3. X-ray diffraction data and structure refinement of compounds 3 and 4

The measurements were performed on an Oxford Xcalibur Gemini, Eos CCD diffractometer with graphite-monochromated CuKα ($\lambda$ = 1.54184 Å) radiation. X-ray diffraction intensities were collected ($\omega$ scans with $\vartheta$ and $\kappa$-offsets), integrated and scaled with CrysAlisPro [19] suite of programs. The unit cell parameters were obtained by least-squares refinement (based on the angular settings for all collected reflections with intensities larger than seven times the standard deviation of measurement errors) using CrysAlisPro.

Data were corrected empirically for absorption employing the multi-scan method implemented in CrysAlisPro. The structures were solved by direct methods with the SHELXS program of the suite SHELX package [20] and the corresponding molecular models developed by alternated cycles of Fourier methods and full-matrix least-squares refinement with SHELXL of the same suit of program.

All hydrogen atoms were located in a difference Fourier map phased on the heavier atoms and refined at their found positions with isotropic displacement parameters. The optimized methyl H-positions converged to staggered conformations. Crystal data and structure refinement results for both compounds are summarized in Table 1. Crystallographic structural data have been deposited at the Cambridge Crystallographic Data Centre (CCDC). Enquiries for data can be direct to: Cambridge Crystallographic Data Centre, 12 Union Road, Cambridge, UK, CB2 1EZ or (e-mail) deposit@ccdc.cam.ac.uk or (fax) +44 (0) 1223 336033. Any request to the Cambridge Crystallographic Data Centre for this material should quote the full literature citation and the reference number CCDC 1541924 (**3**) and CCDC 1541925 (**4**).

## 2.4. Computational details

Theoretical calculations were performed using the Gaussian 03 program [21]. Them were based on the gradient corrected Density Functional Theory (DFT) with the three-parameter hybrid functional (B3) [22] for the exchange part and the Lee-Yang-Parr (LYP) correlation function [23]. Scans of the potential energy curves were carried out at the B3LYP/6-31G (d,p) approximation. Final molecular conformation optimizations and vibration frequencies were computed employing the 6-311++G (d,p) basis set. The calculated vibrational properties correspond, in all cases, to potential energy minima with no imaginary values for the frequencies. Electronic transitions were calculated within the Time-Dependent Density Functional Theory (TD-DFT) [24] in gas phase and taking into account implicitly the solvent effect (ethanol) at B3LYP/6-311 + G (2d,p) approximation. The $^1$H and $^{13}$C NMR chemical shifts were calculated at the B3LYP/6-311 + G (2d,p) level by the gauge-including atomic orbital (GIAO) method [25] using the corresponding TMS shielding, calculated at the same level of theory. The natural bond orbital (NBO) analysis for the molecules was performed at B3LYP/6-311++G (d,p) approximation by means the NBO 3.1 program implemented in the Gaussian 03 package.

## 2.5. Hirshfeld surface analysis

Hirshfeld surfaces and their associated 2D fingerprint plots were constructed using CrystalExplorer 3.1 software [26]. The 3D $d_{norm}$ surfaces were mapped over a fixed color scale of −0.24 (red) to 0.93 Å (blue). Molecular Hirshfeld surfaces in the crystal structure are constructed taking into account the electron distribution calculated as the sum of spherical atom electron densities [27,28]. The Hirshfeld surface enclosing a molecule is defined by points where the contribution to the electron density from the molecule of interest is equal to the contribution from all the other molecules. For each point on that isosurface two distances are defined: $d_e$, the distance from the point to the nearest nucleus external to the surface, and $d_i$ the distance to the nearest nucleus internal to the surface. The normalized contact distance ($d_{norm}$) based on both $d_e$ and $d_i$ and the vdW radii of the atom, given by eq. (1) enables identification of the regions of particular importance to intermolecular interactions [28]. A color scale of red (shorter than vdW separation)-white (equal to vdW separation)-blue (longer than vdW separation) was used to visualize the intermolecular contacts.

$$d_{norm} = \frac{d_i - r_i^{vdW}}{r_i^{vdW}} + \frac{d_e - r_e^{vdW}}{r_e^{vdW}} \tag{1}$$

The combination of $d_e$ and $d_i$ in the form of a 2D fingerprint plot provides summary of intermolecular contacts in the crystal [27]. The 2D fingerprint plots were displayed by using the translated 0.6–2.6 Å range and including reciprocal contacts.

**Table 1**
Crystal data and structure refinement results for compounds **3** and **4**.

| Compound | (**3**) | (**4**) |
|---|---|---|
| Empirical formula | $C_{13} H_{16} O_3$ | $C_{13} H_{16} O_3$ |
| Formula weight | 220.26 | 220.26 |
| Temperature (K) | 293 (2) | 293 (2) |
| Wavelength (Å) | 1.54184 | 1.54184 |
| Crystal system | Triclinic | Monoclinic |
| Space group | P-1 | $P2_1/c$ |
| Unit cell dimensions | | |
| a (Å) | 6.4289 (6) | 11.2891 (6) |
| b (Å) | 8.7120 (6) | 9.1902 (4) |
| c (Å) | 10.952 (1) | 12.4272 (7) |
| α (°) | 92.280 (7) | 90.00 |
| β (°) | 95.738 (7) | 113.689 (7) |
| γ (°) | 103.973 (7) | 90.00 |
| Volume (Å$^3$) | 590.96 (9) | 1180.7 (1) |
| Z, calculated density (Mg/m$^3$) | 2, 1.238 | 4, 1.239 |
| Absorption coefficient (mm$^{-1}$) | 0.708 | 0.708 |
| F (000) | 236 | 472 |
| Crystal size (mm$^3$) | 0.142 × 0.238 × 0.312 | 0.138 × 0.289 × 0.368 |
| ϑ-range (°) for data collection | 5.24 to 70.99 | 4.28 to 72.33 |
| Index ranges | −7 ≤ h ≤ 7, −9 ≤ k ≤ 10, −13 ≤ l ≤ 10 | −13 ≤ h ≤ 11, −10 ≤ k ≤ 11, −15 ≤ l ≤ 15 |
| Reflections collected | 3525 | 4677 |
| Independent reflections | 2247 [R (int) = 0.0176] | 2300 [R (int) = 0.0223] |
| Observed reflections [I > 2σ(I)] | 1817 | 1930 |
| Completeness (%) | 98.3 (to ϑ = 70.99°) | 98.7 (to ϑ = 72.33°) |
| Refinement method | Full-matrix least-squares on F$^2$ | Full-matrix least-squares on F$^2$ |
| Data/restraints/parameters | 2247/0/209 | 2300/0/209 |
| Goodness-of-fit on F$^2$ | 1.046 | 1.053 |
| Final R indices[a] [I > 2σ(I)] | R1 = 0.0477, wR2 = 0.1338 | R1 = 0.0422, wR2 = 0.1158 |
| R indices (all data) | R1 = 0.0567, wR2 = 0.1481 | R1 = 0.0503, wR2 = 0.1264 |
| Largest diff. peak and hole (e.Å$^{-3}$) | 0.193 and −0.185 | 0.164 and −0.206 |

[a] $R_1 = \Sigma ||F_o|-|F_c||/\Sigma|F_o|$, $wR_2 = [\Sigma w (|F_o|^2-|F_c|^2)^2/\Sigma w (|F_o|^2)^2]^{1/2}$.

## 3. Results and discussion

### 3.1. Description of X-ray crystal structure of compounds 3 and 4

ORTEP [29] plots of solid state compounds **3** and **4** are displayed in Fig. 1 and their X-ray geometrical parameters such as bond lengths, angles and dihedral angles, together with the computed values at B3LYP/6-311++G (d,p) approximation are shown in Tables 1 and 2, respectively. Observed bond lengths and angles agree with Organic Chemistry's rules. In particular, C—C bond lengths in the phenyl ring are in the range from 1.367 (2) to 1.401 (2) Å in **3** and from 1.378 (2) to 1.406 (2) Å in **4**, as expected for a resonant bond structure. Single C—C bond distances are in the range from 1.485 (2) to 1.536 (2) Å for **3** and in the 1.483(2)-1.532(2) Å interval for **4**. C=O distance in the ketone group is 1.213 (2) Å for **3** and 1.222 (2) Å for **4**. Hetero-cycle ring C (sp$^2$)-O and O—C (sp$^3$) bond lengths are respectively 1.356 (2) and 1.464 (2) Å in **3**, and 1.356 (2) and 1.467 (2) Å in **4**. All the geometrical parameters related to the chromane moiety are in accordance with the values previously reported for 6-acetyl-2,2-dimethyl-chromane [9].

In the structure of **3**, each molecule participates in four hydrogen bonds and these inter-molecular interactions necessarily dominate the crystal packing of the compound. In the crystal packing of **3**, neighboring molecules related by a unit cell translation along c-axis are linked to each other through inter-molecular O—H···O (keto) bonds [d (OH···O) = 2.014 Å, angle (O—H···O) = 171.7°] giving rise to a polymeric structure along the crystal c-axis (See Fig. 2). The crystal structure of **3** features the characteristic pattern of the $R_4^4(22)$ cyclic hydrogen bond interaction between the O—H···O (keto) and C—H···O (pyrane). Two molecules are also linked between C—H···O (pyrane) hydrogen bonds into centre-symmetric dimers stacked, giving $R_4^4(8)$ graph-set motif as shown in Fig. 2a.

The supramolecular assembly also includes the existence of one intermolecular C—H···π interaction involving the benzene (Cg2 centroid) ring and the H atom bounded to C (10) as can be seen in Fig. 2b. The C10—H···Cg2 interaction [symmetry code: 2-x,1-y,1-z] forms centre-symmetric dimers with an angle of 172°. The distance

**Table 2**
Experimental and calculated bond lengths (Å), bond angles (°), and dihedral angles (°) for compound **3**.

| Parameters | Compound 3 | |
|---|---|---|
| | Experimental[a] | Calculated[b] |
| *Bond lengths* | | |
| C7—C8 | 1.494 (4) | 1.519 |
| C7=O14 | 1.213 (3) | 1.219 |
| C7—C1 | 1.485 (2) | 1.493 |
| C1—C2 | 1.399 (3) | 1.406 |
| C2—C3 | 1.386 (2) | 1.381 |
| C3—C4 | 1.401 (2) | 1.403 |
| C4—C5 | 1.400 (2) | 1.402 |
| C5—C6 | 1.387 (2) | 1.395 |
| C6—C1 | 1.393 (2) | 1.398 |
| C5—C11 | 1.507 (2) | 1.511 |
| C11—C10 | 1.513 (2) | 1.522 |
| C10—C9 | 1.536 (2) | 1.550 |
| C9—O15 | 1.464 (2) | 1.458 |
| C9—C12 | 1.513 (3) | 1.526 |
| C9—C13 | 1.513 (3) | 1.531 |
| C10—O16 | 1.421 (2) | 1.427 |
| C4—O15 | 1.356 (2) | 1.362 |
| *Bond angles* | | |
| C8—C7—C1 | 119.8 (2) | 118.9 |
| C8—C7=O14 | 120.2 (2) | 120.2 |
| C1—C7=O14 | 120.0 (2) | 120.9 |
| C5—C11—C10 | 112.3 (1) | 111.1 |
| C4—O15—C9 | 117.7 (1) | 118.9 |
| O15—C9—C10 | 107.1 (1) | 107.6 |
| C9—C10—O16 | 111.7 (1) | 112.2 |
| O16—C10—C11 | 107.2 (1) | 107.4 |
| C13—C9—C12 | 112.2 (2) | 111.2 |
| *Dihedral angles* | | |
| C8—C7—C1—C2 | 179.6 (2) | 179.8 |
| C8—C7—C1—C6 | −1.5 (3) | 0.4155 |
| C11—C10—C9—O15 | −60.5 (2) | −60.28 |

[a] Experimental values determined by X-ray diffraction methods.
[b] Calculated at B3LYP/6-311++G (d,p) approximation.

between the H and the Cg2 centroid is 2.964 Å.

In **4** the hydroxyl group serves a double stabilizing function acting as a bifurcate H-bond donor. It forms a weak and bent intra-
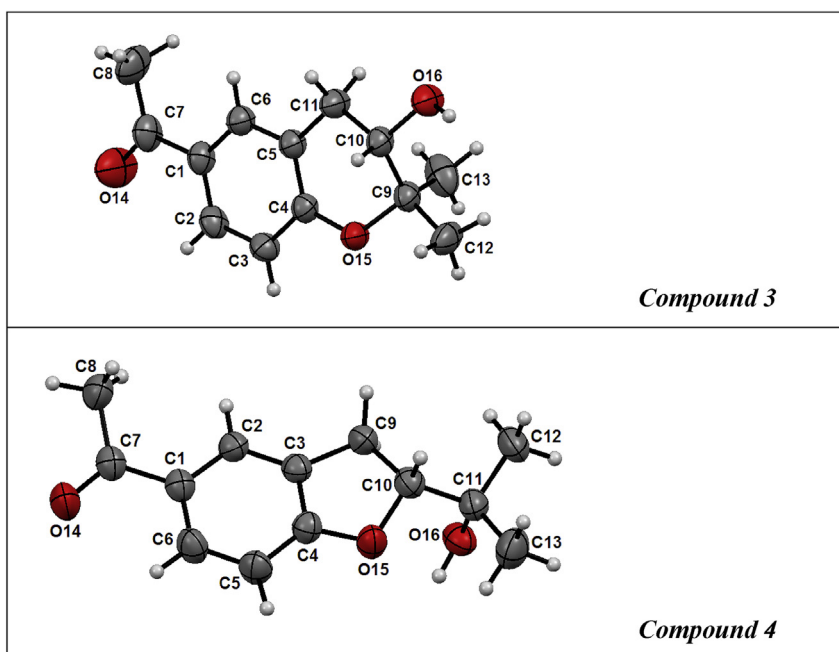


**Fig. 1.** ORTEP drawing of compounds **3** and **4** showing the labels of non-H atoms and their displacement ellipsoids at the 30% probability level.
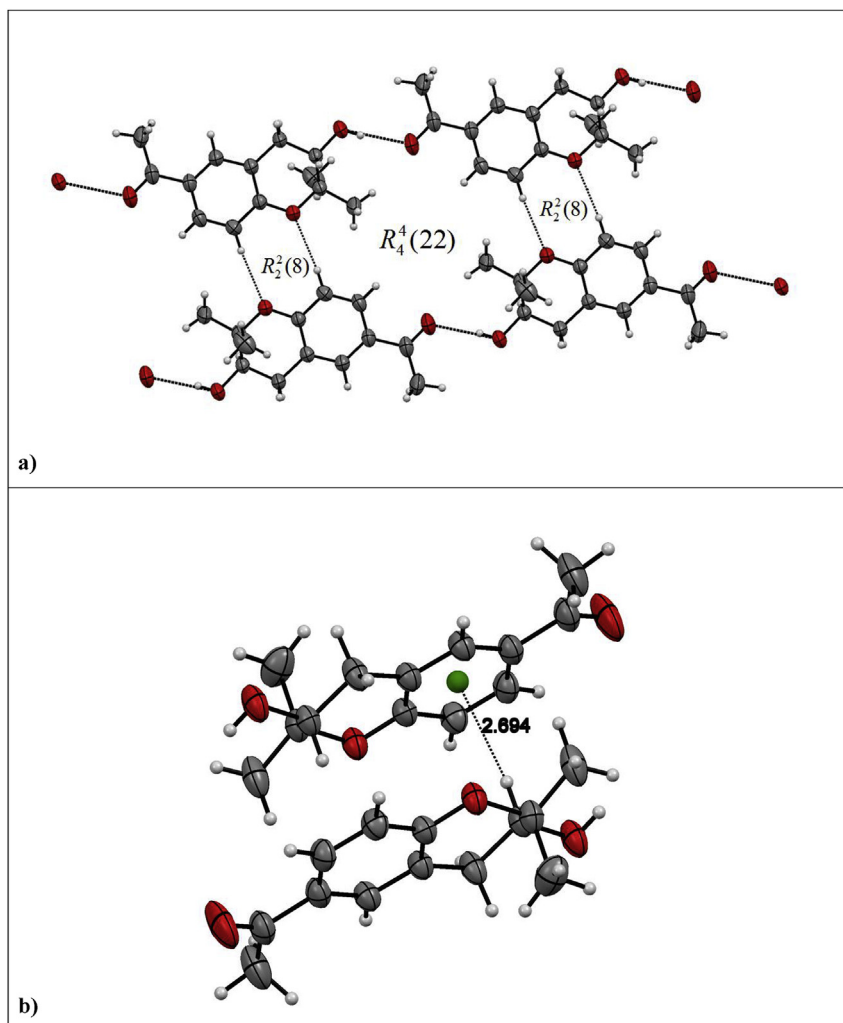
**Fig. 2. (a)** Crystal packing of compound **3** showing centre-symmetric dimers. Intermolecular hydrogen bonds are shown by dashed lines. **(b)** A view of the C−H⋯π interaction showing Cg2 centroid formed by C1 to C6 of the benzene ring.

molecular OH⋯O (furan) bond [d (OH⋯O) = 2.505 Å, ∠(O−H⋯O) = 103.7°] and also links neighboring molecules (symmetry related through a glide plane) to each other by a much stronger inter-molecular O−H⋯O (keto) bond [d (OH⋯O) = 2.051 Å, ∠(O−H⋯O) = 151.8°], giving rise to a zig-zag polymeric structure that extends along the crystal $c$-axis (see Fig. 3).

### 3.2. Hirshfeld surface analysis

Hirshfeld surface analysis was performed to understand the nature of the molecular packing, highlighting the contribution of significant inter-molecular interactions that stabilize the observed crystal structure. Fig. 4 shows the Hirshfeld surfaces ($d_{norm}$ surfaces) of compound **3**. The normalized contact distance ($d_{norm}$) based on both $d_e$ and $d_i$, and the radii of the atom enable the regions indicating the intermolecular interactions. The active spots shown in $d_{norm}$ surfaces characterize the hydrogen-bonding interactions. The large circular spots in deep red, which are visible on the $d_{norm}$ surfaces are an indicator of hydrogen bonding contacts and other visible spots are due to H⋯H interactions. The dominant H⋯O and O⋯H interactions are visualized in Hirshfeld surfaces by the bright red area labeled **1** and **4** in Fig. 4a and b. As was deduced from the crystal structure, these interactions produce a polymeric structure

as can be seen in Fig. 4d. The small amount of area and light color on the surface indicates weaker and longer contacts other than hydrogen bonds. The two red regions labeled **2** and **3** in the $d_{norm}$
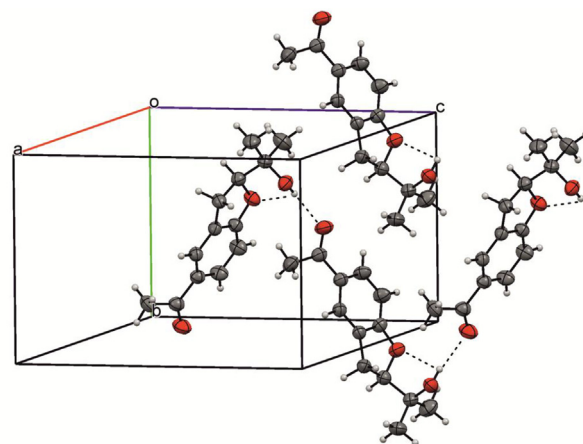


**Fig. 3.** Crystal packing of compound **4** showing a polymeric zig-zag structure along the c-axis. Intra- and inter-molecular interactions are shown in dash lines.
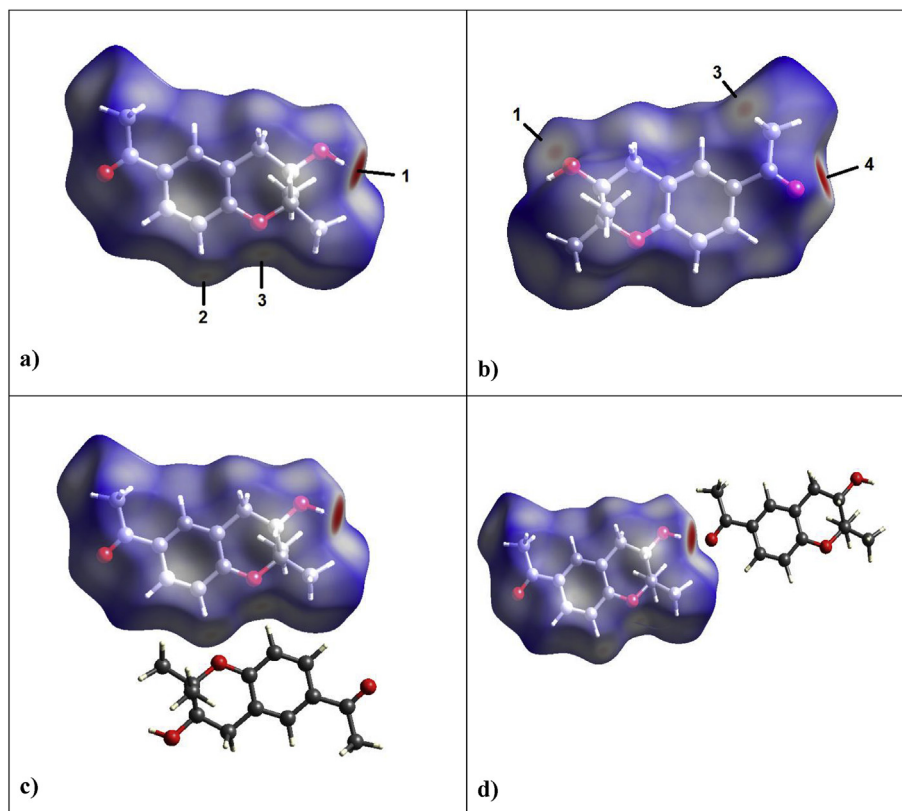
**Fig. 4.** Hirshfeld surface plots ($d_{norm}$) for compound **3**. In the first case, the molecule was rotated by 180° around the horizontal axis of the plot. Thermal ellipsoids drawn at the 50% probability level. Figure labeling is discussed in the text.

map are attributed to C—H···O hydrogen bonds involving the acceptor O15 of the oxopyrane group belonging to two different molecules (see Fig. 4c). The red region located in the methyl groups labeled 3 in Fig. 4b is attributed to C—H···C non-classical hydrogen bonds. The Hirshfeld surfaces mapped with shape index and curvedness for compound **3** are reported in the supplementary material. There is neither touching complementary pair of triangles for shape index surface nor large and green flat regions for curvedness surfaces which indicate that π-π stacking interactions are absent in the crystal packing of compound **3**.

Fig. 5 shows the Hirshfeld surface plots for compound **4**. The spots labeled as **1** and **2**, with the large and circular depressions (deep red) visible on the front and back views of the surfaces are indicative of hydrogen-bonding contacts. These interactions are attributed to O—H···O (keto) interactions. The dominant interactions between C—H and the O atom from the hydroxyl group can be seen in the Hirshfeld surface as the red areas marked as **3** and **4** in Fig. 5. The interaction labeled **3** is assigned to the C—H···O interaction between the hydrogen of the methyl from the acetyl group and the O from the hydroxyl whereas the area marked as **4** is attributed to the interaction between the hydrogen atom from the furan ring and the oxygen from the hydroxyl group. The small extent of area and light color of surface indicates weaker and longer contact other than hydrogen bonds.

Two dimensional (2D) fingerprint plots were obtained by calculating the distances from the Hirshfeld surface to the nearest nucleus inside the surface ($d_i$) to the outs of surface ($d_e$) to analyze the molecular interaction around the nearest neighbor molecules. In 2D plots, green regions show closer contacts and blue color indicates longer contacts. Complementary regions are visible in the fingerprint plots where one molecule acts as donor ($d_e > d_i$) and the other as acceptor ($d_e < d_i$). The fingerprint plots of the main

intermolecular interactions for both structures are shown in Fig. 6. The H···H interaction (labeled as **1**) in compound **3** is 59.2%, whereas in **4** is 59.6%. These interactions have the major contribution to the crystal packing of both structures. The proportion of O···H and H···O interactions (labeled as **2**) comprising 11.8 and 10.0% of the Hirshfeld surface for each molecule of compound **3**. In **3**, the H···O interactions are represented by a spike near a ($d_e + d_i$) sum of 1.85 Å in the bottom left (donor) area of the fingerprint plot (See Fig. 6), which represents the interaction between the hydrogen atom of the hydroxyl group and the carbonyl oxygen. Also, the interaction between oxygen of the pyrane ring interacts with the hydrogen of the benzene ring of another molecule. These interactions produce a three-dimensional network of hydrogen bonds. The O···H interactions are represented by a spike near a ($d_e + d_i$) sum of 1.85 Å in the bottom right (acceptor) region of fingerprint plot, where carbonyl oxygen also acts as acceptor to the neighboring hydrogen atoms from the hydroxyl groups. These interactions represent the closest contacts in the structure and can be seen as a pair of large red spots on the $d_{norm}$ surface (Fig. 4). O···H interactions in compound **4** are represented by spikes near a ($d_e + d_i$) sum of 1.95 Å and represent the interaction between the hydrogen from the hydroxyl group and the O atom from the carbonyl group. The decomposed fingerprint plot shows C—H···C hydrogen bonds of which C—H···π interactions appears as a pair of characteristic wings around ($d_e + d_i$) sum of 3.1 and 3.0 Å in compounds **3** and **4**, respectively. The C···H interactions correspond to 17.4% and 18.3% of total contribution to the Hirshfeld surface for compounds **3** and **4**, respectively.

### 3.3. Structural results derived from quantum chemical calculations

The optimized molecular structures calculated at B3LYP/6-
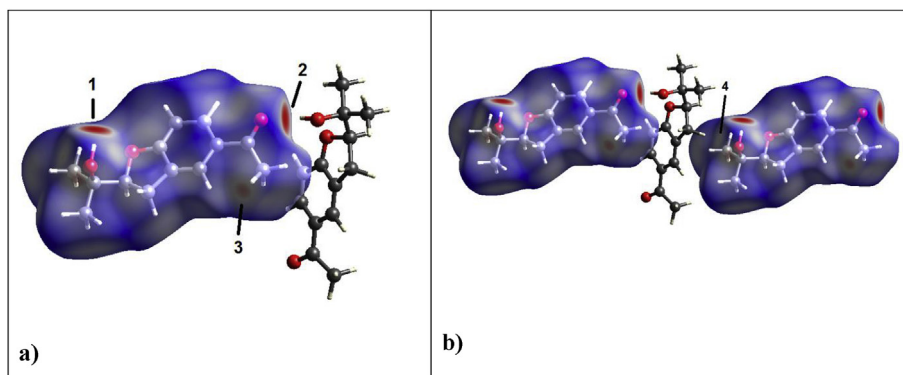
**Fig. 5.** Views of the Hirshfeld surfaces of compound **4** with thermal ellipsoids plotted at 50% level of probability. Labels indicated in the figures are discussed in the text.
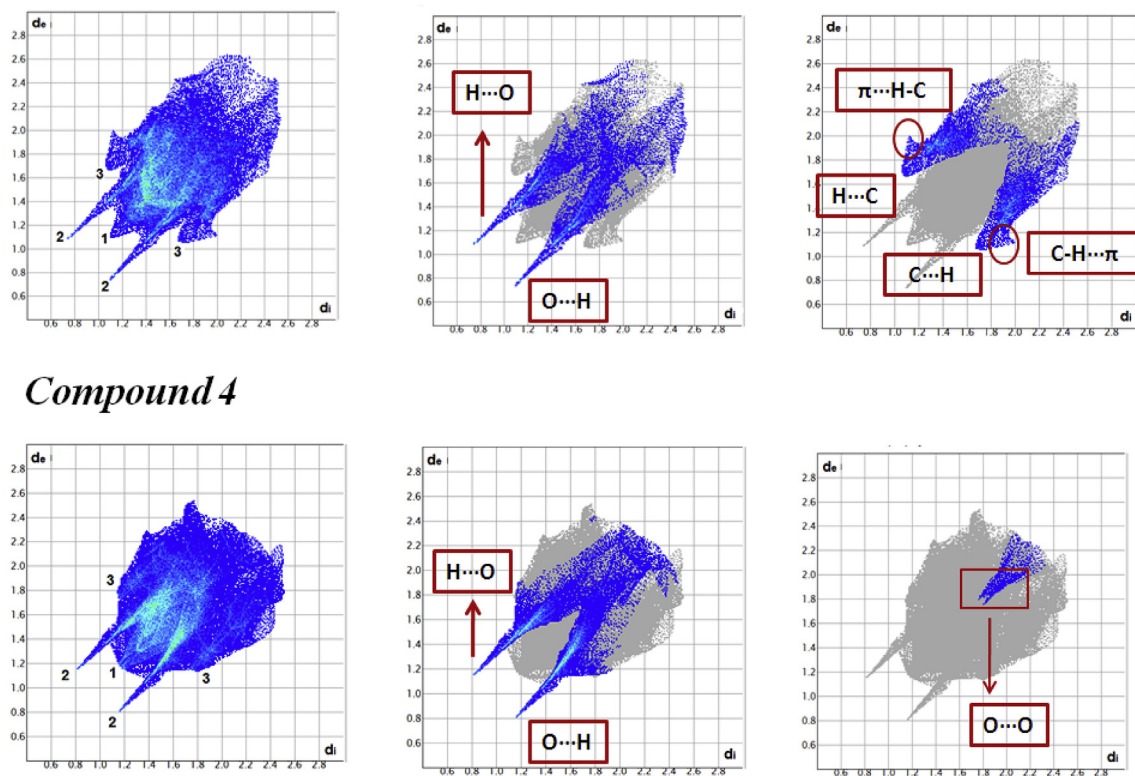


**Fig. 6.** Fingerprint plots for compounds **3** and **4**. Close contacts are labeled as: (1) H···H, (2) O···H and (3) C···H.

311++G (d,p) approximation for compounds **3** and **4** are shown in Fig. 7(a) and (b). The molecules are characterized primarily by a planar conformation. Tables 2 and 3 give a comparison between the

experimental values of the relevant geometrical parameters and the optimized molecular structures calculated at B3LYP/6-311++G (d,p) level. The agreement between the experimental and
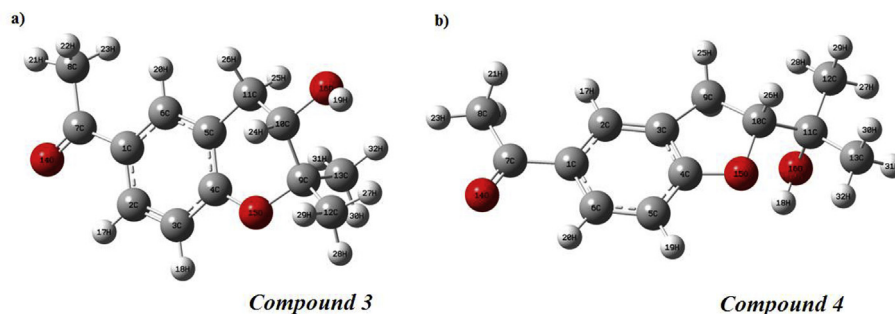


**Fig. 7.** Optimized molecular structures of **3** and **4** calculated at B3LYP/6-311++G (d,p) approximation.

**Table 3**
Experimental and calculated bond lengths (Å), bond angles (°), and dihedral angles (°) for compound **4**.

| Parameters | Compound 4 | |
|---|---|---|
| | Experimental[a] | Calculated[b] |
| *Bond lengths* | | |
| C7−C8 | 1.507 (3) | 1.519 |
| C7=O14 | 1.222 (2) | 1.219 |
| C7−C1 | 1.483 (2) | 1.494 |
| C1−C2 | 1.406 (2) | 1.408 |
| C2−C3 | 1.378 (2) | 1.384 |
| C3−C4 | 1.392 (2) | 1.395 |
| C4−C5 | 1.385 (2) | 1.391 |
| C5−C6 | 1.381 (3) | 1.390 |
| C6−C1 | 1.396 (3) | 1.405 |
| C3−C9 | 1.506 (2) | 1.509 |
| C9−C10 | 1.532 (2) | 1.547 |
| C10−O15 | 1.467 (2) | 1.468 |
| C4−O15 | 1.356 (2) | 1.361 |
| C10−C11 | 1.527 (2) | 1.541 |
| C11−C13 | 1.521 (3) | 1.535 |
| C11−C12 | 1.519 (3) | 1.529 |
| C11−O16 | 1.429 (2) | 1.434 |
| *Bond angles* | | |
| C8−C7−C1 | 118.8 (1) | 118.8 |
| C8−C7=O14 | 120.3 (2) | 120.1 |
| C1−C7=O14 | 120.9 (1) | 121.0 |
| C3−C9−C10 | 102.1 (1) | 102.0 |
| C9−C10−C11 | 116.9 (1) | 116.6 |
| C9−C10−O15 | 105.8 (1) | 105.6 |
| C10−O15−C4 | 107.5 (1) | 107.9 |
| C10−C11−O16 | 109.8 (1) | 109.2 |
| C13−C11−C12 | 110.9 (1) | 110.8 |
| *Dihedral angles* | | |
| C8−C7−C1−C6 | 163.7 (2) | 179.9 |
| C8−C7−C1−C2 | −15.1 (2) | −0.041 |
| C3−C9−C10−O15 | 18.5 (1) | 17.64 |
| C9−C10−C11−O16 | −56.0 (2) | −56.66 |
| O15−C10−C11−O16 | 63.0 (1) | 61.96 |

[a] Experimental values determined by X-ray diffraction methods.
[b] Calculated at B3LYP/6-311++G (d,p) approximation.

computed results is very good in all the groups of the molecules. The small differences between the calculated and experimental geometrical parameters are attributed to the fact that the theoretical calculations were performed with isolated molecules in gas phase whereas the experimental data were based on molecules in the solid state. The acetyl group of molecules **3** and **4** shows only a small distortion from the molecular plane: the C8−C7−C1−C2 and C8−C7−C1−C2 torsion angles are −179.8° and 0.4155°, respectively for compound **3** and -179.9° and −0.041° for compound **4**. The comparison of the X-ray data of compound **3** with those of the parent 6-acetyl-2,2-dimethyl chromane [9] indicates that the presence of the hydroxyl group does not affect the extent of planarity in the phenyl ring and the acetyl group.

The Natural Bond Orbital (NBO) population analysis is an important tool to calculate donor→ acceptor interactions estimated by the second order perturbation theory [30,31]. The lone-pair electron at the carbonyl oxygen atom donates electronic density mainly to the vacant C1−C7 and C7−C8 anti-bonding orbitals via hyper-conjugative interactions of the type $LP_\pi O$ (14)→ σ* C−C with energy values of 20.40 and 21.45 kcal $mol^{-1}$, respectively for compound **3** and 18.52 and 19.97 kcal $mol^{-1}$ for compound **4**. The mesomeric effect, reflected mainly by the $LP_\pi$ O (15) → π* C4−C5 interactions are 28.03 and 28.52 kcal $mol^{-1}$ for compounds **3** and **4**, respectively. This type of interaction also leads to increased occupation numbers of the corresponding π* C4−C5 orbitals. In the case of compound **3**, the occupation number is slightly larger (0.39e) than that in compound **4** (0.38e). The described increased population of the π* C4−C5 orbital in compound **3** reduces the C4−C5 bond strength and, as a consequence, a bond lengthening (See Tables 2 and 3).

The total atomic charges of compounds **3** and **4** are obtained from natural population analysis at B3LYP/6-311++G (d,p) level are provided as Supplementary Information. The atomic charges obtained using the natural population analysis approach revealed that the more negative charge (−0.74 a.u.) is located at the O (16) atom of the hydroxyl group and the negative charges −0.57 and −0.56 are located at the O (15) and O (14) atoms, respectively for compound **3**. Similar results were obtained for compound **4**. The more negative charge on O (16) atom makes C (7) atom more positive and acidic (charge of +0.56). The negative charges mainly located on O (16), O (15) and O (14) atoms could interact with the positive part of a receptor. In addition, C (7) atom is the most positively charged part and could interact with the negatively charged part of a receptor easily.

In order to understand the sites for electrophilic and nucleophilic attacks, we resorted to molecular electrostatic potential (MEP) calculations [32,33]. MEP plots of compounds **3** and **4** generated at the optimized geometry of both molecules using GaussView 05 software are shown in the Supplementary Information. The red and blue regions of MEP represent the net negative and positive charges, respectively. For compound **3**, the red regions are mainly located on the oxygen atom of the carbonyl group and the oxygen atom of the hydroxyl group. The atomic charge analysis and MEP calculation confirmed that hydroxyl and carbonyl oxygen atoms are preferred sites for electrophilic attack. Similar results were obtained for compound **4**. It is evident from the MEP map for compound **3** that the region around the hydrogen atoms of the hydroxyl group is electron deficient (blue region), in accordance with NPA charges with a maximum positive value (0.46) for H (19)
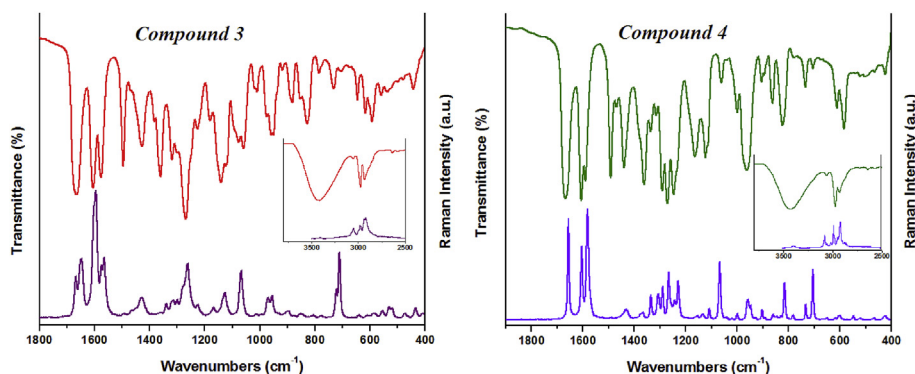


**Fig. 8.** Selected region of the IR and Raman spectra of compounds **3** and **4** in solid state. Inset: IR and Raman spectra of compounds **3** and **4** in the 3800–2500 cm$^{-1}$ region.

**Table 4**
Observed and calculated frequencies (in cm$^{-1}$) and tentative assignments of modes for compound **3**.

| Mode | Experimental | | Calculated[c] | | | Tentative assignment[d,e] |
|------|------------|-----------|----------|--------|--------|---------------------------|
|      | IR (solid)[a] | Raman (solid)[b] | Unscaled | Scaled | IR int |                           |
| 1  | 3427 bd   | –          | 3844 | 3779 | 41  | $\nu$ O−H |
| 2  | –         | 3072 (12)  | 3203 | 3148 | 4   | $\nu$ C−H (R1) |
| 3  | 3056 vw   | 3055 (20)  | 3186 | 3132 | 2   | $\nu$ C−H (R1) |
| 4  | 3051 vw   | 3052 sh    | 3172 | 3118 | 7   | $\nu$ C−H (R1) |
| 5  | –         | 3042 (14)  | 3141 | 3088 | 15  | $\nu_a$ CH$_3$(CO) |
| 6  | –         | –          | 3120 | 3067 | 17  | $\nu_a$ CH$_3$ (R2) |
| 7  | –         | 3003 (15)  | 3112 | 3059 | 25  | $\nu_a$ CH$_3$ (R2) |
| 8  | –         | –          | 3109 | 3056 | 6   | $\nu_a$ CH$_3$ (R2) |
| 9  | –         | 2983 (27)  | 3103 | 3050 | 22  | $\nu_a$ CH$_3$ (R2) |
| 10 | –         | –          | 3090 | 3037 | 9   | $\nu_a$ CH$_3$ (CO) |
| 11 | 2979 w    | 2980 (26)  | 3071 | 3019 | 17  | $\nu_a$ CH$_2$ (R2) |
| 12 | –         | –          | 3045 | 2993 | 10  | $\nu_s$ CH$_3$ (R2) |
| 13 | 2935 w    | 2936 (39)  | 3034 | 2982 | 22  | $\nu_s$ CH$_3$ (R2) |
| 14 | –         | 2924 (41)  | 3033 | 2981 | 4   | $\nu_s$ CH$_3$ (CO) |
| 15 | 2911 sh   | 2916 (37)  | 3027 | 2975 | 18  | $\nu_s$ CH$_2$ (R2) |
| 16 | 2879 sh   | 2891 (19)  | 2996 | 2945 | 24  | $\nu$ C10−H |
| 17 | 1673 s    | 1668 (32)  | 1734 | 1704 | 258 | $\nu$ C=O |
| 18 | 1663 s    | 1648 (46)  | 1644 | 1575 | 106 | $\nu$ C−C (R1) + $\delta$ C−H (R1) |
| 19 | 1604 m    | 1600 (100) | 1606 | 1539 | 142 | $\nu$ C−C (R1) + $\delta$ C−H (R1) |
| 20 | 1576 m    | 1574 (41)  | 1524 | 1459 | 42  | $\delta_a$ CH$_3$ (R2) + $\delta$ C−H (R1) |
| 21 | 1495 m    | –          | 1514 | 1450 | 6   | $\delta_a$ CH$_3$ (R2) |
| 22 | 1434 sh   | –          | 1503 | 1440 | 4   | $\delta_a$ CH$_3$ (R2) |
| 23 | 1427 m    | 1429 (16)  | 1493 | 1430 | 9   | $\delta$ CH$_2$ (R2) + $\delta_a$ CH$_3$ (R2) |
| 24 | –         | –          | 1484 | 1422 | 2   | $\delta_a$ CH$_3$ (R2) + $\delta$ CH$_2$ (R2) |
| 25 | –         | –          | 1482 | 1420 | 2   | $\delta$ CH$_2$ (R2) + $\delta_a$ CH$_3$ (R2) |
| 26 | –         | –          | 1481 | 1419 | 12  | $\delta_a$ CH$_3$ (CO) |
| 27 | –         | –          | 1472 | 1410 | 15  | $\delta_a$ CH$_3$ (CO) |
| 28 | 1383 w    | –          | 1450 | 1389 | 26  | $\nu$ C−C (R1) + $\delta$ C−H (R1) + $\omega$ CH$_2$ |
| 29 | 1366 sh   | –          | 1423 | 1363 | 6   | $\delta$ OCH + $\delta_s$ CH$_3$ (R2) + $\delta$ O−H |
| 30 | 1360 m    | –          | 1415 | 1356 | 14  | $\delta$ C−H (R1) + $\delta_s$ CH$_3$ (R2) |
| 31 | –         | –          | 1402 | 1343 | 22  | $\delta_s$ CH$_3$ (R2) |
| 32 | –         | 1339 (11)  | 1385 | 1327 | 57  | $\delta_s$ CH$_3$(CO) |
| 33 | 1318 w    | 1316 (13)  | 1374 | 1316 | 3   | $\delta$ OCH |
| 34 | 1301 vw   | 1300 (14)  | 1350 | 1293 | 28  | $\nu$ C−C (R1) |
| 35 | 1267 vs   | 1279 (24)  | 1335 | 1279 | 64  | $\delta$ C−H (R1) + $\omega$ CH$_2$ (R2) + $\delta$ O−H |
| 36 | 1251 sh   | 1250 (43)  | 1301 | 1246 | 56  | $\omega$ CH$_2$ (R2) + $\delta$ C−H (R1) |
| 37 | –         | –          | 1286 | 1232 | 85  | $\tau\omega$ CH$_2$ + $\delta$ C−H (R1) + $\delta$ O−H |
| 38 | 1226 w    | 1226 (10)  | 1282 | 1228 | 220 | $\nu$ C4−O15 + $\delta$ C−H (R1) |
| 39 | –         | –          | 1271 | 1218 | 43  | $\delta$ C−H (R2) + $\nu$ C−O + $\rho$ CH$_2$ |
| 40 | –         | –          | 1263 | 1210 | 47  | $\nu$ C9−C10 + $\rho$ CH$_3$ (R2) |
| 41 | 1180 w    | –          | 1221 | 1170 | 63  | $\delta$ COH + $\nu_a$ C(CH$_3$)$_2$ |
| 42 | –         | 1169 (8)   | 1190 | 1140 | 1   | $\nu$ C5−C11 + $\delta$ C−H (R1) |
| 43 | 1140 m    | 1143 sh    | 1168 | 1119 | 153 | $\rho$ CH$_2$ + $\rho$ CH$_3$ (R2) |
| 44 | 1122 m    | 1127 (19)  | 1162 | 1113 | 6   | $\rho$ CH$_3$ (R2) + $\delta$ C−H (R1) |
| 45 | 1089 sh   | –          | 1134 | 1086 | 103 | $\delta$ C−H (R1) |
| 46 | 1077 w    | –          | 1092 | 1046 | 6   | $\rho$ CH$_3$(CO) + $\delta$ C−H (R1) |
| 47 | –         | 1068 (37)  | 1079 | 1034 | 157 | $\nu$ C10−O16 |
| 48 | 1059 w    | –          | 1055 | 1011 | 4   | $\nu$ C9−C10 + $\delta$ O−H |
| 49 | 1010 vvw  | –          | 1042 | 998  | 1   | $\rho$ CH$_3$(CO) |
| 50 | 975 vw    | 970 (16)   | 1027 | 984  | 16  | $\rho$ CH$_3$ (R2) |
| 51 | 958 w     | 955 (17)   | 996  | 954  | 3   | $\gamma$ C−H (R1) |
| 52 | 948 w     | –          | 988  | 947  | 19  | $\gamma$ C−H (R1) |
| 53 | 937 sh    | 930 (3)    | 961  | 920  | 48  | $\nu$ C9−O15 + $\rho$ CH$_3$(R2) + $\gamma$ C−H (R1) |
| 54 | 917 vvw   | 913 (3)    | 959  | 919  | 69  | $\nu$ C7−C8 + $\rho$ CH$_3$(CO) |
| 55 | –         | 898 (5)    | 943  | 903  | 7   | $\nu_s$ C(CH$_3$)$_2$ |
| 56 | 881 w     | –          | 929  | 889  | 3   | $\delta$ CCC (R1) + $\gamma$ C−H (R1) |
| 57 | –         | –          | 903  | 865  | 8   | $\gamma$ C−H (R1) |
| 58 | 853 vw    | 852 (3)    | 886  | 849  | 12  | $\nu$ C9−O15 |
| 58 | 829 w     | –          | 853  | 817  | 29  | $\gamma$ C−H (R1) |
| 60 | 785 vw    | 780 (2)    | 792  | 759  | 3   | $\delta$ O15−C9−C12 + $\delta$ CCC (R1) |
| 61 | 732 vw    | 722 (41)   | 745  | 714  | 2   | $\gamma$ CCC (R1) + $\gamma$ C−H (R1) |
| 62 | –         | 710 (52)   | 732  | 701  | 3   | $\delta$ CCC (R1) + $\nu_s$ C(CH$_3$)$_2$ |
| 63 | 703 vw    | –          | 713  | 683  | 1   | $\delta$ COC (R2) |
| 64 | 646 vw    | 641 (2)    | 652  | 625  | 11  | $\delta$ CCC (R1) + $\delta$ CCC (R2) |
| 65 | 617 vw    | 612 (2)    | 626  | 600  | 8   | $\gamma$ C=O + $\gamma$ CCC (R1) + $\gamma$ C−H (R1) |
| 66 | 592 vw    | 590 (3)    | 611  | 585  | 26  | $\delta$ CC=O + $\delta$ CCC (R1) |
| 67 | 560 vvw   | 556 (5)    | 555  | 532  | 1   | $\delta$ CCC (R2) |
| 68 | 536 vvw   | 531 (9)    | 531  | 509  | 10  | $\delta$ C10−C9−C12 |
| 69 | 524 sh    | 520 (8)    | 524  | 502  | 3   | $\gamma$ CCC (R1) + $\gamma$ C=O |
| 70 | 479 vvw   | 474 (3)    | 500  | 479  | 6   | $\delta$ CCC (R1) |
| 71 | –         | –          | 454  | 435  | 1   | $\gamma$ CCC (R1) + $\gamma$ C−H (R1) |
| 72 | 443 vw    | 435 (8)    | 442  | 423  | 5   | $\delta$ COC (R2) + $\delta$ C(CH$_3$)$_2$ |
| 73 | –         | 408 (3)    | 427  | 409  | 1   | $\delta$ CCO (R2) + $\delta$ C8−C7−C1 |

(continued on next page)

**Table 4** (*continued*)

| Mode | Experimental | | Calculated[c] | | | Tentative assignment[d,e] |
|---|---|---|---|---|---|---|
| | IR (solid)[a] | Raman (solid)[b] | Unscaled | Scaled | IR int | |
| 74 | – | 388 (4) | 413 | 396 | 12 | $\delta$ C8—C7—C1 + $\gamma$ COC (R2) |
| 75 | – | 375 (5) | 364 | 349 | 1 | $\delta$ C(CH$_3$)$_2$ |
| 76 | – | 304 (6) | 315 | 302 | 2 | $\gamma$ CCC (R2) + $\gamma$ O—H |
| 77 | – | – | 296 | 284 | 1 | $\tau$ CH$_3$ (R2) |
| 78 | – | – | 294 | 282 | 36 | $\gamma$ O—H |
| 79 | – | 262 (8) | 276 | 264 | 14 | $\tau$ O—H |
| 80 | – | – | 270 | 259 | 56 | $\tau$ CH$_3$ (R2) + $\tau$ O—H |
| 81 | – | – | 254 | 243 | 4 | $\tau$ C9—C10 |
| 82 | – | 222 (9) | 236 | 226 | 14 | $\tau$ CH$_3$ (R2) |
| 83 | – | – | 217 | 208 | <1 | $\tau$ CH$_3$ (R2) + $\tau$ O—H |
| 84 | – | 176 (20) | 192 | 184 | 3 | $\tau$ C5—C11 + $\tau$ CH$_3$ (R2) |
| 85 | – | – | 142 | 139 | 1 | $\tau$ CH$_3$(CO) |
| 86 | – | – | 140 | 134 | 2 | $\tau$ CH$_3$(CO) |
| 87 | – | 125 (42) | 125 | 120 | 1 | $\tau$ CCCC (R1) + $\tau$ CCCC (R2) |
| 88 | – | – | 105 | 101 | 1 | $\tau$ CCCC (R1) + $\tau$ COCC (R2) |
| 89 | – | – | 50 | 48 | 4 | $\tau$ C7—C1 |
| 90 | – | – | 46 | 44 | 1 | $\tau$ CCOC (R2) |

[a] sh: shoulder, s: strong, w: weak, m: medium, v: very.
[b] Relative band heights in parenthesis.
[c] Calculated at B3LYP/6-311++G (d,p) approximation. Scale factor used 0.983 for frequencies higher than 1700 cm$^{-1}$ and 0.958 for frequencies lower than 1700 cm$^{-1}$.
[d] $\nu$: stretching, $\delta$: in-plane bending, $\gamma$: out-of-plane bending, $\rho$: rocking, $\omega$: wagging, $\tau\omega$: twisting, $\tau$: torsional modes.
[e] See Fig. 7 for atoms numbering scheme. R1: benzene ring, R2: pyrane ring.

atom. The blue region is also observed around the hydrogen atom of the hydroxyl group in compound **4**.

### 3.4. Vibrational results

The FTIR and Raman spectra for the solid sate compounds **3** and **4** are shown in Fig. 8. The observed and computed frequencies (B3LYP/6-311++G (d,p)), together with the corresponding assignment of bands, are given in Tables 4 and 5. A tentative assignment of the observed bands in the IR and Raman spectra were carried out by comparison with theoretical results and also with the frequencies reported for related compounds. A very good agreement between the experimental and calculated vibration data was observed. Only the normal modes of the most relevant characteristic functional groups of the molecules will be discussed.

#### 3.4.1. Assignment of bands

3.4.1.1. OH modes. For compound **3**, the very broad IR absorption band centered at 3427 cm$^{-1}$ is assigned to the O—H stretch. This mode was calculated at 3844 cm$^{-1}$ at the B3LYP/6-311++G (d,p) approximation. For compound **4**, this mode appears as a broad band located at 3435 cm$^{-1}$ in the IR spectrum and at 3389 cm$^{-1}$ in Raman. The strong hydrogen bonding present in the solid state of this compound red-shifts the $\upsilon$(O—H) frequency. The O—H in-plane bending mode is observed in the IR spectra at 1180 cm$^{-1}$ (**3**) and 1292 cm$^{-1}$ (**4**). This mode appears at 1289 cm$^{-1}$ in the Raman spectrum of compound **4**. The calculated frequencies for both compounds appear in Tables 4 and 5.

3.4.1.2. CH$_3$ modes. The Raman dispersion bands observed at 3042, 3003 and 2983 cm$^{-1}$ in compound **3** are assigned to CH$_3$ asymmetric stretching modes. In compound **4** these bands appear at 2976 cm$^{-1}$ in the IR spectrum and at 3045, 3006, 2977, 2968 and 2915 cm$^{-1}$ in Raman. For **3** the CH$_3$ symmetric stretching modes are observed at 2935 cm$^{-1}$ in the IR spectrum and at 2936 and 2924 cm$^{-1}$ in Raman. For compound **4**, the bands located at 2909 and 2865 cm$^{-1}$ in the Raman spectrum are assigned to the mode previously mentioned. The CH$_3$ asymmetric bending modes are observed in the IR spectra as medium-intensity bands at 1576, 1495 and 1434 cm$^{-1}$ for **3** and as medium-intensity bands at 1469 and 1440 cm$^{-1}$ for **4**. These frequencies are in accordance with the data

reported in literature [9,34]. For **3**, the Raman dispersion band located at 1339 cm$^{-1}$ is assigned to the CH$_3$ symmetric bending mode. For compound **4**, the bands corresponding to the CH$_3$ symmetric bending mode are well defined in the IR and Raman spectra. This vibration appears at 1380, 1362 and 1314 cm$^{-1}$ in IR and at 1382 and 1367 cm$^{-1}$ in Raman. The IR bands located at 1122, 1077, 1010 and 975 cm$^{-1}$ in compound **3** (1127 cm$^{-1}$ in Raman) are assigned to the CH$_3$ rocking mode. For **4**, these vibrations appear at 1020 and 999 cm$^{-1}$ in IR and at 1042, 1023 and 999 cm$^{-1}$ in Raman. This assignment was in accordance with literature data [9,34] and it is supported by quantum chemical calculations (see Tables 4 and 5).

3.4.1.3. CH$_2$ modes. The CH$_2$ stretching modes are observed in the IR spectrum of **3** as a weak band located at 2979 cm$^{-1}$ and as a low-intensity Raman band at 2980 cm$^{-1}$. A similar feature was observed for compound **4**, in which the weak IR band located at 2935 cm$^{-1}$ (2939 cm$^{-1}$ in Raman) is assigned to the previously mentioned mode. The shoulder observed in the IR spectrum of **3** at 2911 cm$^{-1}$ (2916 cm$^{-1}$ in Raman) is assigned to the CH$_2$ symmetric stretching mode. This mode was not detected in the IR and Raman spectra of compound **4**. The medium-intensity band located at 1427 cm$^{-1}$ in the IR spectrum of **3** is assigned to the CH$_2$ bending mode. For compound **4**, this vibration appears as a Raman band located at 1429 cm$^{-1}$. The modes corresponding to the wagging, twisting and rocking modes of the methylene group are all assigned and given in Tables 4 and 5.

3.4.1.4. CH modes. The aromatic structure gives rise to C—H stretching vibrations in the frequency region from 3200 to 3000 cm$^{-1}$. These modes are not affected by the nature and position of substituents. In both compounds, two rings are fused together and three C—H stretching vibrations are expected. The characteristic C—H stretching mode for compound **3** is assigned to the very weak IR bands observed at 3056 and 3951 cm$^{-1}$ and at 3072, 3055 and 3052 cm$^{-1}$ in Raman. This assignment is in accordance with the theoretical predictions (see Table 4). For compound **4**, the C—H stretching vibration appears as low-intensity bands in the Raman spectrum at 3068, 3062 and 3051 cm$^{-1}$.

In compound **3**, the IR spectrum shows two absorptions at 1360 and 1267 cm$^{-1}$, with medium and very strong intensities, respectively, which are assigned to the in-plane C—H bending modes of

**Table 5**
Observed and calculated frequencies (in cm$^{-1}$) and tentative assignments of modes for compound **4**.

| Mode | Experimental | | Calculated[c] | | | Tentative assignment[d,e] |
|---|---|---|---|---|---|---|
| | IR (solid)[a] | Raman (solid)[b] | Unscaled | Scaled | IR int | |
| 1 | 3435 bd | – | 3802 | 3737 | 24 | ν O–H |
| 2 | 3065 w | 3068 (17) | 3203 | 3149 | 4 | ν C–H (R1) |
| 3 | – | 3062 (8) | 3189 | 3135 | 1 | ν C–H (R1) |
| 4 | – | 3051 (5) | 3183 | 3129 | 6 | ν C–H (R1) |
| 5 | – | 3045 (6) | 3142 | 3089 | 14 | ν$_a$ CH$_3$(CO) |
| 6 | – | 3006 (8) | 3116 | 3063 | 33 | ν$_a$ CH$_3$ |
| 7 | – | – | 3112 | 3059 | 17 | ν$_a$ CH$_3$ |
| 8 | 2976 m | 2977 (30) | 3109 | 3056 | 22 | ν$_a$ CH$_3$ |
| 9 | – | 2968 (13) | 3098 | 3045 | 15 | ν$_a$ CH$_3$ |
| 10 | 2935 w | 2939 (14) | 3091 | 3038 | 12 | ν$_a$ CH$_2$ |
| 11 | – | 2915 (30) | 3090 | 3037 | 8 | ν$_a$ CH$_3$ (CO) |
| 12 | – | 2909 (34) | 3042 | 2990 | 27 | ν$_s$ CH$_3$ |
| 13 | – | – | 3040 | 2988 | 9 | ν$_s$ CH$_2$ |
| 14 | – | – | 3033 | 2981 | 11 | ν$_s$ CH$_3$ (CO) |
| 15 | – | 2965 (7) | 3032 | 2980 | 15 | ν$_s$ CH$_3$ + ν$_s$ CH$_3$ (CO) |
| 16 | – | 2850 (7) | 3015 | 2974 | 19 | ν C10–H |
| 17 | 1668 s | 1656 (92) | 1735 | 1706 | 246 | ν C=O |
| 18 | 1607 vs | 1604 (66) | 1643 | 1574 | 111 | ν C–C (R1) + δ C–H (R1) |
| 19 | 1589 s | 1582 (100) | 1622 | 1554 | 117 | ν C–C (R1) |
| 20 | 1491 m | 1490 (3) | 1519 | 1455 | 79 | ν C–C (R1) + δ C–H (R1) |
| 21 | 1469 w | – | 1513 | 1449 | 6 | δ$_a$ CH$_3$ |
| 22 | 1440 m | 1445 (6) | 1502 | 1439 | 3 | δ$_a$ CH$_3$ |
| 23 | – | 1434 (10) | 1490 | 1427 | 3 | δ$_a$ CH$_3$ + δ CH$_2$ |
| 24 | – | 1429 (8) | 1485 | 1423 | 5 | δ CH$_2$ |
| 25 | – | 1418 sh | 1481 | 1419 | 12 | δ$_a$ CH$_3$ (CO) |
| 26 | – | – | 1481 | 1419 | 1 | δ$_a$ CH$_3$ |
| 27 | – | – | 1472 | 1410 | 16 | δ$_a$ CH$_3$ (CO) |
| 28 | – | – | 1461 | 1399 | <1 | ν C–C (R1) + δ C–H (R1) |
| 29 | 1380 sh | 1382 (3) | 1423 | 1363 | 18 | δ$_s$ CH$_3$ |
| 30 | 1362 m | 1367 (7) | 1404 | 1345 | 18 | δ$_s$ CH$_3$ |
| 31 | 1336 w | 1336 (22) | 1391 | 1333 | 30 | δ$_s$ OCH + δ$_s$ CH$_3$ |
| 32 | 1314 w | – | 1386 | 1328 | 60 | δ$_s$ CH$_3$(CO) + δ C–H (R1) |
| 33 | – | 1307 (24) | 1367 | 1310 | 24 | δ C9C10–H |
| 34 | 1292 m | 1289 (31) | 1357 | 1300 | 40 | δ COH + δ$_s$ CH$_3$(CO) |
| 35 | 1270 s | 1266 (43) | 1335 | 1279 | 19 | δ COH + δ OCH |
| 36 | – | – | 1311 | 1256 | 87 | ω CH$_2$ (R2) + δ C–H (R1) |
| 37 | 1247 m | 1243 (18) | 1286 | 1232 | 230 | ω CH$_2$ + ν C1–C7 |
| 38 | 1235 m | 1229 (35) | 1263 | 1210 | 162 | δ C–H (R1) + ω CH$_2$ |
| 39 | – | – | 1259 | 1206 | 16 | δ C–H (R1) + τω CH$_2$ + δ OCH |
| 40 | 1164 m | 1166 (3) | 1248 | 1196 | 71 | ν C10–C11 + ρ CH$_3$ |
| 41 | 1156 sh | 1153 (4) | 1214 | 1163 | 5 | ν$_a$ C(CH$_3$)$_2$ + δ CH (R1) + τω CH$_2$ |
| 42 | – | 1135 (5) | 1180 | 1130 | 57 | ν$_s$ C(CH$_3$)$_2$ + δ C–H (R1) + τω CH$_2$ |
| 43 | 1123 m | – | 1177 | 1128 | 15 | δ C–H (R1) |
| 44 | 1112 m | 1109 (10) | 1140 | 1092 | 33 | δ C–H (R1) |
| 45 | 1061 w | 1067 (53) | 1134 | 1086 | 103 | ν$_a$ C(CH$_3$)$_2$ + δ COH + ρ CH$_3$ |
| 46 | – | 1042 (3) | 1078 | 1033 | 18 | ρ CH$_3$(CO) + δ C–H (R1) |
| 47 | 1020 sh | 1023 (2) | 1051 | 1007 | 4 | ν C9–C10 + ρ CH$_3$ |
| 48 | 999 w | 999 (5) | 1042 | 998 | 1 | ρ CH$_3$ |
| 49 | 962 s | 958 (18) | 1022 | 979 | 16 | ρ CH$_2$ + ρ CH$_3$ + ν C10–O15 |
| 50 | – | 948 (13) | 992 | 950 | 4 | γ C–H (R1) + ν C9–C10 |
| 51 | – | – | 987 | 946 | 6 | γ C–H (R1) |
| 52 | – | 929 (2) | 967 | 926 | 73 | ν$_a$ C10–C11–O16 + ρ CH$_3$ |
| 53 | – | – | 960 | 920 | 27 | ν$_s$ C10–C11–O16 + ρ CH$_3$ |
| 54 | 904 w | 903 (9) | 955 | 915 | 105 | ν C7–C8 + ρ CH$_3$(CO) |
| 55 | 894 vw | 892 (2) | 939 | 900 | 2 | ν$_a$ C11–C12–C13 |
| 56 | 861 m | 860 (5) | 915 | 877 | 3 | δ CCC (R1) + γ C–H (R1) |
| 57 | – | 846 (3) | 906 | 868 | 7 | γ C–H (R1) |
| 58 | 822 m | 830 (4) | 866 | 829 | 20 | ν$_a$ C10–C11–C13 + ρ CH$_3$ |
| 58 | 813 sh | 815 (34) | 849 | 813 | 37 | γ C–H (R1) |
| 60 | 781 vvw | 783 (5) | 830 | 795 | 4 | δ OCC (R2) + δ CCC (R1) |
| 61 | 734 w | 733 (14) | 791 | 758 | 9 | ν$_s$ C13–C11–C10 + δ CCC (R2) |
| 62 | 705 vw | 706 (46) | 748 | 717 | 4 | γ CCC (R1) + γ C–H (R1) |
| 63 | – | 651 (2) | 714 | 636 | 2 | δ CCC (R1) + ν C–C (R2) |
| 64 | 611 m | 618 (2) | 664 | 636 | 3 | δ OCC (R2) + ρ CH$_2$ |
| 65 | – | 600 (4) | 627 | 601 | 1 | δ CCC (R1) + δ CCC(R2) |
| 66 | – | – | 619 | 593 | 11 | γ C=O + γ C–H (R1) |
| 67 | 583 m | – | 605 | 580 | 43 | δ C=O + δ CCO |
| 68 | – | 548 (4) | 555 | 532 | 4 | δ C13–C12–C11 + δ CCC (R1) |
| 69 | 523 vvw | 520 (1) | 525 | 503 | 3 | γ CCC (R1) + γ C–H (R1) |
| 70 | 504 vvw | – | 524 | 502 | 3 | γ CCC (R1) |
| 71 | 465 vvw | 468 (1) | 463 | 444 | 7 | δ C8C7C1 + δ C12C11O16 |
| 72 | 423 vw | 427 (3) | 431 | 413 | 6 | γ CCC (R1) |
| 73 | – | – | 418 | 400 | 9 | γ CO–H |

**Table 5** (*continued*)

| Mode | Experimental | | Calculated[c] | | | Tentative assignment[d,e] |
|------|-------------|-------------|--------|--------|--------|----------------------------|
| | IR (solid)[a] | Raman (solid)[b] | Unscaled | Scaled | IR int | |
| 74 | – | 394 (1) | 415 | 398 | 170 | $\gamma$ CO—H |
| 75 | – | 371 (1) | 387 | 371 | 10 | $\delta$ C12-11-O16 |
| 76 | – | – | 365 | 350 | 5 | $\delta$ C10—C11—C12 |
| 77 | – | 325 (5) | 319 | 306 | 5 | $\gamma$ CCC (R1) |
| 78 | – | 291 (5) | 309 | 296 | 1 | $\gamma$ C12C11O16 |
| 79 | – | – | 292 | 280 | 1 | $\tau$ CH$_3$ |
| 80 | – | 254 (6) | 250 | 240 | 0 | $\tau$ CH$_3$ |
| 81 | – | 224 (10) | 245 | 235 | 0 | $\tau$ R2 |
| 82 | – | 206 (5) | 218 | 209 | 9 | $\tau$ R2 + $\tau$ CH$_3$ |
| 83 | – | – | 213 | 204 | 2 | $\tau$ CH$_3$ |
| 84 | – | – | 187 | 179 | 2 | $\delta$ C7C1C2 |
| 85 | – | 137 (24) | 149 | 143 | <1 | $\tau$ CH$_3$(CO) |
| 86 | – | – | 126 | 121 | 3 | $\tau$ R1 |
| 87 | – | – | 106 | 102 | 1 | $\tau$ COCC (R2) |
| 88 | – | – | 77 | 74 | <1 | $\tau$ C10—C11 |
| 89 | – | – | 50 | 48 | 5 | $\tau$ C7—C1 |
| 90 | – | – | 39 | 37 | 1 | $\tau$ R2 |

[a] sh: shoulder, s: strong, w: weak, m: medium, v: very.

[b] Relative band heights in parenthesis.

[c] Calculated at B3LYP/6-311++G (d,p) approximation. Scale factor used 0.983 for frequencies higher than 1700 cm$^{-1}$ and 0.958 for frequencies lower than 1700 cm$^{-1}$.

[d] $\nu$: stretching, $\delta$: in-plane bending, $\gamma$: out-of-plane bending, $\rho$: rocking, $\omega$: wagging, $\tau\omega$: twisting, $\tau$: torsional modes.

[e] See Fig. 7 for atoms numbering scheme. R1: benzene ring, R2: furan ring.

the aromatic ring. The Raman dispersion counterpart appears at 1279 cm$^{-1}$. For compound **4**, the in-plane C—H stretching modes appear as medium-intensity IR bands at 1235, 1123 and 1112 cm$^{-1}$ (1229 and 1109 cm$^{-1}$ in Raman). The out-of-plane C—H deformation modes are all assigned in Tables 4 and 5.

*3.4.1.5. C=O modes.* For **3**, the strong IR absorption at 1673 cm$^{-1}$ (calculated value at 1734 cm$^{-1}$) is attributed to the $\upsilon$(C=O) mode. This vibration corresponds to the medium-intensity Raman band observed at 1668 cm$^{-1}$. In compound **4**, the $\upsilon$(C=O) mode appears as a strong IR band at 1668 cm$^{-1}$ and the Raman counterpart at 1666 cm$^{-1}$. The spectral features and assignment of the C=O in-plane and out-of-plane bending vibrations for compounds **3** and **4** are included in Tables 4 and 5, respectively.

### 3.5. Electronic spectra and frontier molecular orbitals

The experimental (measured in ethanol solvent) and calculated electronic absorption spectra of compounds **3** and **4** are shown in the Supplementary Information. The assigned transitions with major contributions for both compounds are shown in Table 6. A very good correlation between experimental and calculated spectra was observed. In the experimental spectrum, the two bands centered at 280 and 289 nm are assigned to the HOMO→LUMO transitions for **3** and **4**, respectively. The bands corresponding

**Table 6**
Experimental and calculated absorption wavelengths and oscillator strengths for compounds **3** and **4**.

| Wavelength (nm) | | Oscillator strength | Assignment |
|-----------------|-----------|--------------------|------------|
| Experimental | Calculated | | |
| **Compound 3** | | | |
| – | 314 | 0.0002 | HOMO-1→LUMO (98%) |
| 280 | 286 | 0.4265 | HOMO→LUMO (100%) |
| – | 270 | 0.0354 | HOMO-2→LUMO (66%) |
| | | | HOMO →LUMO+1 (31%) |
| **Compound 4** | | | |
| – | 315 | 0.0001 | HOMO-1→LUMO (97%) |
| 289 | 278 | 0.3696 | HOMO→LUMO (96%) |
| – | 260 | 0.0254 | HOMO-2→LUMO (54%) |
| | | | HOMO→LUMO+1 (44%) |

to the HOMO-2→LUMO and HOMO→LUMO+1 were not observed experimentally due to their lower oscillator strength (see Table 6).

The frontier molecular orbitals involved in the electronic transitions for compounds **3** and **4** are depicted in Fig. 9. As can be observed in Fig. 9, the HOMO for both compounds involves $\pi$-bonding orbitals of the aromatic ring and the non-bonding character of the three oxygen and some carbon atoms from another ring. The LUMO exhibits a $\pi$ anti-bonding character of the carbon atoms of the aromatic ring and non-bonding character of some carbon atoms of the pyran and furan rings. Thus, the HOMO-→LUMO transition has a $\pi \rightarrow \pi^*$ nature. The HOMO-1 corresponds to a *p*-type orbital strongly located on the oxygen atom of the carbonyl group and the carbon atoms of the acetyl group. The HOMO-2 corresponds to a $\pi$-bonding system located over the aromatic ring and a p-type orbital located on the oxygen and a carbon atom of the hetero-cycle ring. In LUMO+1 the electron density of $\pi^*$ nature is extended all over the aromatic ring.

### 3.6. $^1$H NMR spectral study

The $^1$H NMR spectra of the title compounds have been recorded in CDCl$_3$ and the chemical shifts for non-equivalent protons relative to TMS are given in the experimental section (Section 3.1). The signals due to the characteristic aromatic protons were observed in the region 7.83—7.81 ppm. For compound **3**, the signals located at 7.75, 7.73 and 6.85 are assigned to H-7, H-5, H-8, respectively. The $^1$H NMR spectra of compound **4** shows two doublets at 7.81 and 6.82 ppm due to H-6 and H-7, respectively. The signal corresponding to H-4 appears as a singlet at 7.83 ppm.

The two doublets located at 3.10 and 2.83 ppm in the $^1$H NMR spectra of compound **3**, are attributed to H-4 of the pyran ring and the doublet at 3.22 ppm observed in compound **4** is assigned to H-3 corresponding to the benzofuran ring. The protons H-9 corresponding to the CH$_3$(CO) group appears as a singlet at 2.54 ppm. The signals observed at 1.38 and 1.35 ppm in the spectra of compound **3** are assigned to each gem-dimethyl group. The $^1$H NMR spectra of compound **4** show two singlets at 1.25 and 1.23 ppm due to H-4′ and H-5′, respectively. The total of protons calculated from the integration curve is in accordance with those calculated from the proposed molecular formula.
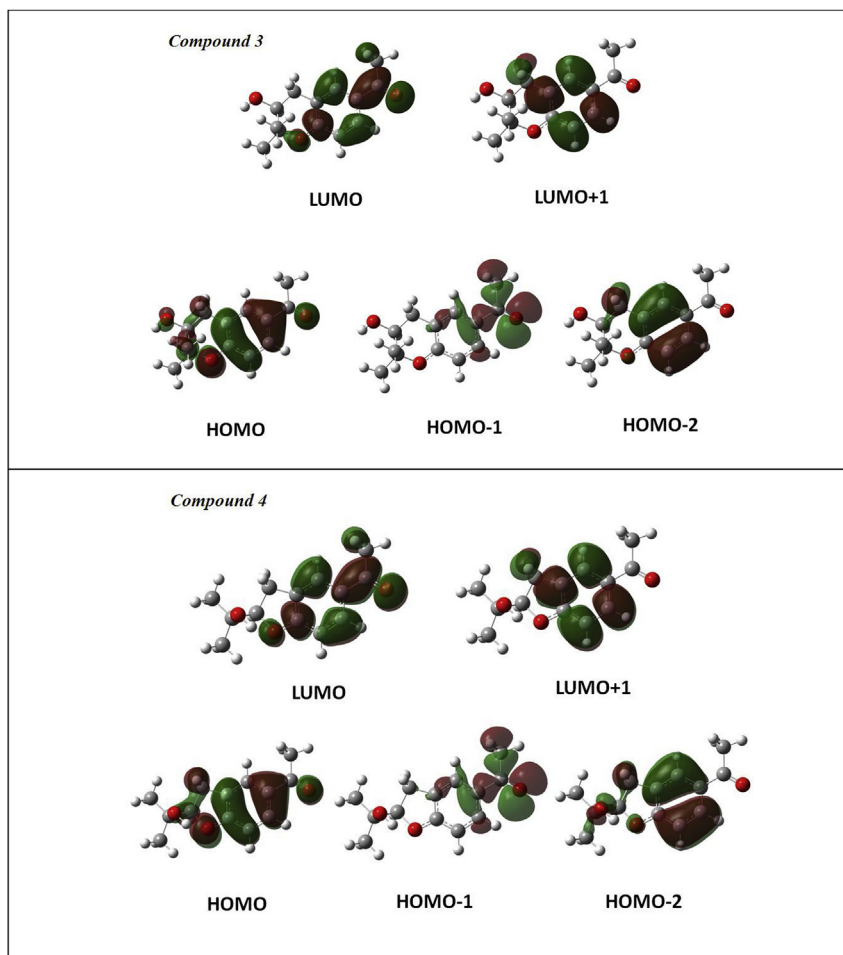
**Fig. 9.** Frontier molecular orbitals involved in the main electronic transitions of compounds **3** and **4**.

## 4. Conclusions

The benzopyran 2,2-dimethyl-3-hydroxy-6-acetyl-chromane (compound **3**) and benzofuran 10,11-dihydro-10-hydroxytremeto-ne (compound **4**) are structural isomers that biogenetically are formed from a prenylated *p*-hydroxyacetophenone precursor. The crystal structure of both substances was determined by X-ray diffraction methods and the major packing interactions that help to stabilize each structure were identified. Compound **3** crystallizes in the triclinic P-1 space group and compound **4** in the monoclinic $P2_1/c$ space group. The Hirshfeld surfaces and fingerprint plots were used to understand, identify and quantify the interactions that are responsible for different packing patterns observed in both compounds. In accordance with Hirshfeld surface analysis, the relative contributions of H···H interactions are higher than other contacts. Intra- and inter-molecular hydrogen bonding interactions play a dominant role in structural diversity related to different kinds of supra-molecular assembly of both compounds. The theoretical results agree with the experimental observations. The vibrational and electronic properties were fully determined by combining experimental data and quantum chemical calculations.

## Appendix A. Supplementary data

Supplementary data related to this article can be found at http://dx.doi.org/10.1016/j.molstruc.2017.05.137.

## References

[1] P. Proksch, E. Rodriguez, Phytochemistry 22 (1983) 2335.
[2] E. Romano, A. Raschi, A.M. González, G. Jaime, M. Fortuna, R. Hernández, H. Bach, A. Benavente, Plant Physiol. Biochem. 49 (2001) 671.
[3] K.C. Nicolaou, J.A. Pfefferkorn, A.J. Roecker, G.Q. Cao, S. Barluenga, H.J. Mitchell, J. Am. Chem. Soc. 122 (2000) 9939.
[4] L. Li, H.-K. Wang, J.-J. Chang, A.T. McPhail, D.R. McPhail, H. Terada, T. Konoshima, M. Kokumai, M. Kozuka, K.-H. Lee, J. Nat. Prod. 56 (1993) 690.
[5] S. Kawaii, Y. Tomono, E. Katase, K. Ogawa, M. Yano, Y. Takemura, M. Ju-ichi, C. Ito, H. Furukawa, J. Nat. Prod. 62 (1999) 587.
[6] S.P. Pillai, S.R. Menon, L.A. Mitscher, C.A. Pillai, D.M. Shankel, J. Nat. Prod. 62 (1999) 1358.
[7] Y. Kashman, K.R. Gustafson, R.W. Fuller, J.H. Cardellina, J.B. McMahon, M.J. Currens, R.W. Buckheit, S.H. Hughes, G.M. Cragg, M.R. Boyd, J. Med. Chem. 35 (1992) 2735.
[8] A.D. Patil, A.J. Freyer, D.S. Eggleston, R.C. Haltiwanger, M.F. Bean, P.B. Taylor, M.J. Caranfa, A.L. Breen, H.R. Bartus, J. Med. Chem. 36 (1993) 4131.
[9] E. Lizarraga, D.M. Gil, G.A. Echeverría, O.E. Piro, C.A.N. Catalán, A. Ben Altabef, Spectrochim. Acta A 127 (2014) 74.
[10] L. Tsung-Jen, E. Ramstad, P. Heinstein, Phytochemistry 13 (1974) 1809.
[11] R. Siebertz, P. Proksch, L. Witte, Phytochemistry 29 (1990) 2135.
[12] R. Siebertz, P. Proksch, V. Wray, L. Witte, Phytochemistry 28 (1989) 789.
[13] L. Margl, C. Ettenhuber, I. Gyurjan, M.H. Zenk, A. Bacher, W. Eisenreich, Phytochemistry 66 (2005) 887.
[14] T. Garcia de Quesada, B. Rodriguez, S. Valverde, Phytochemistry 11 (1972) 446.
[15] F. Bohlmann, C. Zdero, R.M. King, H. Robinson, Phytochemistry 19 (1980)

1141.

[16] S. Piacente, R. Aquino, N. De Tommasi, O. Lock De Ugaz, H. Chavez Orellana, Phytochemistry 31 (1992) 2182.

[17] J.R. Soberón, E. Lizarraga, M.A. Sgariglia, M.B. Carrasco Juárez, D.A. Sampietro, A. Ben Altabef, C.A.N. Catalán, M.A. Vattuone, Ant. van Leeuwenhoek J. Microbiol. 108 (2015) 1047—1057.

[18] T. Tomas-Barberán, E. Iniesta-Sanmartin, F. Tomás-Lorente, A. Rumbero, Phytochemistry 29 (1990) 1093.

[19] CrysAlisPro, Oxford Diffraction Ltd., version 1.171.33.48 (release 15-09-2009CrysAlis171.NET).

[20] G.M. Sheldrick, Acta Crystallogr. A64 (2008) 112.

[21] M.J. Frisch, J.A. Pople, J.S. Binkley, J. Chem. Phys. 80 (1984) 3265. M. J. Frisch, G. W. Trucks, H. B. Schlegel, G. E. Scuseria, M. A. Robb, J. R. Cheeseman, J. A. Montgomery Jr., T. Vreven, K. N. Kudin, J. C. Burant, J. M. Millam, S. S. Iyengar, J. Tomasi, V. Barone, B. Mennucci, M. Cossi, G. Scalmani, N. Rega, G. A. Petersson, H. Nakatsuji, M. Hada, M. Ehara, K. Toyota, R. Fukuda, J. Hasegawa, M. Ishida, T. Nakajima, Y. Honda, O. Kitao, H. Nakai, M. Klene, X. Li, J. E. Knox, H. P. Hratchian, J. B. Cross, C. Adamo, J. Jaramillo, R. Gomperts, R. E. Stratmann, O. Yazyev, A. J. Austin, R. Cammi, C. Pomelli, J. W. Ochterski, P. Y. Ayala, K. Morokuma, G. A. Voth, P. Salvador, J. J. Dannenberg, V. G. Zakrzewski, S. Dapprich, A. D. Daniels, M. C. Strain, O. Farkas, D. K. Malick, A. D. Rabuck, K.

Raghavachari, J. B. Foresman, J. V. Ortiz, Q. Cui, A. G. Baboul, S. Clifford, J. Cioslowski, B. B. Stefanov, G. Liu, A. Liashenko, P. Piskorz, I. Komaromi, R. L. Martin, D. J. Fox, T. Keith, M. A. Al-Laham, C. Y. Peng, A. Nanayakkara, M. Challacombe, P. M. W. Gill, B. Johnson, W. Chen, M. W. Wong, C. González, J. A. Pople, Gaussian 03, revision C.02; Gaussian, Inc.: Wallingford, CT, 2004.

[22] A.D. Becke, J. Chem. Phys. 98 (1993) 5648.

[23] C. Lee, W. Yang, R.G. Parr, Phys. Rev. B 37 (1988) 785.

[24] P. Elliot, F. Furche, K. Burke, Rev. Comp. Chem. 26 (2009) 91.

[25] J.R. Cheeseman, G.W. Trucks, T.A. Keith, M.J. Frisch, Chem. Phys. 104 (1996) 5497.

[26] J.J. McKinnon, M.A. Spackman, A.S. Mitchel, Acta Crystallogr. B60 (2004) 627.

[27] M.A. Spackman, P.G. Byrom, Chem. Phys. Lett. 267 (1997) 215.

[28] M.A. Spackman, J.J. McKinnon, CrystEngComm 4 (2002) 378.

[29] L.J. Farrugia, J. Appl. Cryst. 30 (1997) 565.

[30] A.E. Reed, L.A. Curtis, F. Weinhold, Chem. Rev. 88 (1988) 899.

[31] J.P. Foster, F. Weinhold, J. Am. Chem. Soc. 102 (1980) 7211.

[32] N. Okulik, A.H. Jubert, Internet Electron J. Mol. Des. 4 (2005) 17.

[33] J. Sponer, P. Hobza, Int. J. Quantum Chem. 57 (1996) 959.

[34] D. Lin-Vien, N.B. Colthup, W.G. Fateley, J.G. Grasselli, The Handbook of Infrared and Raman Characteristic Frequencies of Organic Molecules, Academic Press, Inc, United Kingdom, 1991.